

PAPER

Enhancing single-shot fringe pattern phase demodulation using advanced variational image decomposition

To cite this article: Maria Cywiska *et al* 2019 *J. Opt.* **21** 045702

View the [article online](#) for updates and enhancements.



IOP | ebooks™

Bringing you innovative digital publishing with leading voices to create your essential collection of books in STEM research.

Start exploring the collection - download the first chapter of every title for free.

Enhancing single-shot fringe pattern phase demodulation using advanced variational image decomposition

Maria Cywińska^{1,3} , Maciej Trusiak^{1,3} , Chao Zuo² and Krzysztof Patorski¹

¹Warsaw University of Technology, Institute of Micromechanics and Photonics, Warsaw, Poland

²Jiangsu Key Laboratory of Spectral Imaging & Intelligence Sense, Nanjing University of Science and Technology, Nanjing, Jiangsu Province 210094, People's Republic of China

E-mail: mcywinska.mchtr@gmail.com and m.trusiak@mchtr.pw.edu.pl

Received 12 December 2018, revised 5 February 2019

Accepted for publication 15 February 2019

Published 18 March 2019



CrossMark

Abstract

In many full-field optical metrology techniques, i.e. interferometry, moiré, and structured light, the information about the measurand, e.g. displacement, strain, or 3D shape, is stored in the phase distribution of a recorded two-dimensional intensity pattern—the fringe pattern. Its analysis (phase demodulation) therefore plays a crucial role in the measurement procedure, significantly affecting the total accuracy of the optical system. Phase demodulation methods based on just a single fringe pattern are especially interesting, due to their robustness to environmental disturbances and ability to examine dynamic events. However, the calculated phase map is easily spoiled by errors, which appear mainly because of fringe pattern imperfections, i.e. random noise, parasitic interferences, a nonsinusoidal fringe pattern profile or a non-uniform image background. In this contribution, an advanced variational image decomposition scheme is proposed to reduce these phase demodulation errors. The reported purely phase domain method can be easily adopted to aid virtually any fringe analysis method, including single-frame and multi-frame phase-shifting, possibly enhancing retrieved phase distribution without the need for hardware manipulation. We employed it to improve single-frame Hilbert–Huang transform-based fringe analysis. The remarkable efficiency and versatility of the developed algorithm are verified by processing synthetic and experimental fringe patterns and phase maps. The demonstrated approach compares favorably with the very capable 2D empirical mode decomposition reference method.

Keywords: interferometry, fringe analysis, phase measurement, phase retrieval, phase imaging, phase enhancement

1. Introduction

When performing full-field optical measurements using interferometry, moiré, structured light, holography, etc, one often encounters the measurand encoded in a fringe pattern [1–3]. In numerical analysis, the pattern undergoes the phase demodulation routine to retrieve the information of interest. It can be seen as a transition from the fringe intensity domain into the phase domain. The fringe pattern phase can be associated with the local shape, orientation, and spatial

frequency of fringes. This transition is usually performed using the multi-frame phase-shifting approach, requiring appropriate hardware and software and thus limiting the measurement time resolution. Therefore, very accurate and capable phase-shifting techniques do not fully cover dynamic events. Single-frame techniques are employed for transient event characterization. Their errors strongly depend on algorithmic solutions applied for single fringe pattern processing. The Fourier transform (FT) method [4] is very popular but has limitations in terms of the carrier spatial frequency and global spectrum filtering. The FT localized relatives, such as the windowed Fourier transform [5],

³ Authors to whom any correspondence should be addressed.

S-transform [6], and continuous wavelet transform (CWT) [7], or other approaches including shearlet transform [8], spatial carrier phase-shifting [9], and regularized phase tracking [10], are generally very capable but require a set of parameters to be fixed. They can be computationally and algorithmically demanding, and exhibit characteristic errors (e.g. the CWT method introduces errors in areas of strong phase gradients correctable for an especially tailored numerical scheme). A similar remark may be made about the recently introduced continuous phase estimation method based on the implicit smoothing splines [11], which needs a valid starting point (phase initial guess) if it is to perform correctly.

Recently, the 2D Hilbert–Huang transform (HHT) was proposed for phase extraction from fringe patterns [12–17]. The 2D Hilbert transform [15–18] introduces numerically a $\pi/2$ phase shift to the original fringe pattern. In this straightforward way, a 2D complex analytic signal (with the original fringe pattern as the real part and its Hilbert transform as the imaginary part) is created, with easy access to its phase and amplitude distributions by computing the angle and modulus of a complex image. The HHT is a fast, adaptive and accurate approach, not strictly limited in carrier frequency and robust to fringe defects due to Huang’s empirical mode decomposition adaptive band-pass pre-filtering. The original fringe image needs background rejection to enable an efficient 2D Hilbert transformation. It is implemented by subtracting its last several decomposition components. The first empirical mode (or several first modes) of the original fringe pattern can be associated with noise and eliminated in a denoising procedure.

Every single-frame fringe demodulation method (and especially the 2D Hilbert transform) has three strong error sources, i.e. the noise (including parasitic interference fringes), the fringe background term [15–17], and the non-sinusoidal fringe waveform [1, 19]. Strong background variations and nonlinearly projected fringes (more historically recorded fringes) introduce errors regardless of the optical measurement technique (e.g. interferometry, structured illumination, moiré, holography) and the selected single-frame phase demodulation strategy. Moreover, in phase-shifting schemes, a change of background intensity between the images and the nonlinear fringe profile also cause a decrease in accuracy [1–3, 20]. The errors produced appear as residual fringes in an unwrapped phase map (a fringe-like periodic phase error [19, 20]). High-frequency noise transfers from fringe intensity into phase domain, often causing serious problems with phase unwrapping [21]. Parasitic interference fringes originating from spurious reflections in an optical setup also contribute to the final phase map deterioration.

In this contribution, without a loss of generality, we focus on phase error reduction in the single-frame phase demodulation techniques exemplified by the HHT [15–17]. The novel approach presented deploys variational image decomposition (VID) [22–25] previously used for fringe pre-filtering. The similarity and difference between fringe and phase filtration will be discussed in section 2. A straightforward yet very

efficient and important modification has been incorporated into the classical VID algorithm, thus creating an advanced image decomposition method (modified VID, mVID). By ‘modification’, we mean the introduction of a tolerance parameter as a single and universal determinant for the end of the decomposition, understood as a stopping criterion for the iterative minimization algorithm used in VID to estimate the fringe part. VID filtration can be successfully applied to virtually any unwrapped phase map demodulated by one of the various single-frame, two-image and multi-interferogram methods. The proposed technique is validated in comparison with the reference method—advanced fast and adaptive bidimensional empirical mode decomposition (AFABEMD) [14, 16, 17]. Both are image processing tools working in the image domain (in our case, it is the unwrapped phase map domain) without resorting to any transformation or the need of hardware modifications.

The proposed processing path, presented in figure 1, can be expressed in the following steps:

1. fringe pattern pre-filtering using the AFABEMD method (background and noise rejection);
2. pre-filtered fringe pattern phase demodulation, using the 2D Hilbert spiral transform;
3. phase map enhancement using the proposed advanced VID method (compared with the AFABEMD reference technique).

Steps 1 and 2 comprise an already established HHT procedure, whereas step 3 is the main novelty of this paper. It is worth emphasizing that other phase demodulation techniques can be implemented, replacing HHT.

The paper is structured as follows: section 2 describes the HHT-based single-frame phase demodulation and the reference AFABEMD methods, section 3 introduces the mVID technique, section 4 contains numerical simulations evaluating the proposed HHT-mVID phase calculation method, section 5 presents experimental validation, and section 6 concludes the paper.

2. The Hilbert–Huang transform-based single-frame phase demodulation

A cosinusoidal waveform fringe pattern can be generally described as

$$I(x, y) = a(x, y) + b(x, y)\cos(p(x, y)) + n(x, y), \quad (1)$$

where a , b , p , and n denote background, amplitude modulation, phase distribution, and noise, respectively. The reduction of phase errors can be initiated before phase demodulation by fringe pattern background elimination (a), neglecting higher harmonics and parasitic interferences (stored together with high-frequency noise) and contrast normalization ($b = 1$). In an ideal result, we have a perfect fringe pattern with phase function modulating the argument of the cosine function

$$I_F(x, y) = \cos(p(x, y)). \quad (2)$$

In the 2D HHT, the 2D empirical mode decomposition (EMD) based techniques (Huang's part of the transform) were successfully employed for fringe pattern pre-filtering [12–17]. VID can serve this purpose as well [22–25]. Residual pre-processing imperfections affect the demodulated phase distribution calculated using the 2D Hilbert spiral transform (HST) [17–20], however. The HST computes a quadrature component (I_Q) to the filtered fringe pattern (I_F):

$$\begin{aligned} I_Q(x, y) &= HST(I_F(x, y)) \\ &= -i \exp(-i\beta) F^{-1} \\ &\quad \times \{P(\zeta_1, \zeta_2) F[I_F(x, y)]\} \\ &= -\sin(p(x, y)). \end{aligned} \quad (3)$$

Here, β denotes a fringe orientation map, F and F^{-1} denote forward and inverse Fourier transforms, and $P(\zeta_1, \zeta_2)$ denotes spiral phase function formulate in spectral coordinates as:

$$P(\zeta_1, \zeta_2) = \frac{\zeta_1 + i\zeta_2}{\sqrt{\zeta_1^2 + \zeta_2^2}}. \quad (4)$$

In other words, the HST creates a 2D analytic pattern with its real part defined as a filtered fringe pattern (I_F) and its imaginary part as its quadrature component (I_Q). Phase is calculated using the arctangent function to determine the angle of the 2D analytic pattern:

$$p(x, y) = \text{angle}(I_F + iI_Q). \quad (5)$$

The HST is extremely sensitive to a locally non-zero mean value of the filtered fringe pattern [17–20], whereas noise transfers freely from intensity to phase domain. Therefore, it is of the utmost importance to remove the fringe pattern background accurately and possibly minimize noise. It is worth noting that the fringe pattern contrast normalization is a nonlinear operation [14–18], resulting in higher harmonics (fringe nonlinearity) generation. The same phase errors are introduced by projector (more historically by detector) nonlinearities or a non-zero spatially varying background. Fringe nonlinearities and non-zero background induced errors cause the appearance of residual fringes in the resultant phase distribution. They can also originate from spurious reflections in optical setup and parasitic interferences.

Improvement of the quality of the demodulated phase map can be accomplished by a sine/cosine technique [26] and fringe pattern filtration algorithms. Nevertheless, in the case of sine/cosine filtering, we cannot simply remove the texture part of the variational image decomposition because all the information in this case is there (fringes contain the phase information of interest and cannot be removed upon neglecting texture). The consequence is the impossibility of minimizing fringe-like errors introduced by either insufficient background removal or introduced nonlinearity using sine/cosine filtering, although it works perfectly for phase map denoising (the removal of high-frequency random noise).

We propose to correct the residual fringes and noise present in the unwrapped phase domain by advancing the VID approach. Error reduction after demodulation is quite different from that before phase calculation (in the fringe pattern intensity domain). Now we have calculated phase distribution

φ with its fundamental ideal component (p) mixed with residual fringes and noise κ :

$$\varphi(x, y) = \kappa(x, y) + p(x, y). \quad (6)$$

We aim at residual fringes and noise, $\kappa(x,y)$, extraction for their elimination from the unwrapped phase, $\varphi(x,y)$. We want to preserve 'true phase' constituting the fundamental term of the calculated phase, $p(x,y)$. In fringe preprocessing the component to be preserved is the one containing the middle part of the spatial frequency bandwidth (fringes), and the terms to be filtered out are low spatial frequency background and high spatial frequency noise. In the phase error minimization procedure, the part to be preserved—'true phase'—can be considered as the lower spatial frequency component, and we aim at the residual fringes and noise removal. Residual noise, not filtered in pre-processing, also undergoes elimination in the proposed mVID phase domain filtering procedures. Prior to introducing the mVID method we briefly describe the reference technique we use for comparison, the AFABEMD method, a recent image processing technique already successfully applied in fringe analysis.

Empirical mode decomposition was proposed by Norden Huang as a 1D signal processing tool [27]. Based on the extrema distribution, it adaptively decomposes a signal into sub-signals oscillating in various scales. Managing the set of intrinsic mode functions (IMFs; sub-signals, modes), one can create an efficient processing tool. In this work we use the 2D AFABEMD algorithm [14, 16, 17] as a reference technique. Image two-dimensional empirical mode decomposition is combined with the 2D HST, creating the HHT. Essentially, each decomposed bidimensional component (2D IMF, BIMF) has the zero mean value necessary for efficient HST demodulation. An uneven background spoils the demodulated phase more severely than fringe profile nonlinearities. AFABEMD decomposes an image into a set of BIMFs using order-statistic filtering. Introducing instead the morphological strategy employed in enhanced fast empirical mode decomposition (EFEMD) [14, 17] developed in our group, we could gain computational speed acceleration. It is worth noting that EFEMD produces fewer modes than AFABEMD. A high 'mode resolution' combined with high decomposition speed provides the driving force to propose AFABEMD as a reference technique. It works in image domain just like mVID, and is a software-oriented phase enhancement technique not resorting to any hardware modifications.

A short description of the AFABEMD processing path is as follows:

1. initialization of the image (fringe pattern in the case of fringe pattern filtration, and unwrapped phase in the case of phase enhancement) and detection of image extrema;
2. calculation of the shortest distance D between two adjacent extrema, and creation of a morphological structuring element, i.e. a disk of diameter D ;
3. estimating an upper (and lower) envelope using the mathematical morphology operation of grayscale

- dilation employed using the structuring element to the image (and reversed image);
4. calculating the mean envelope as the arithmetic mean of lower and upper envelopes;
 5. smoothing the mean envelope using an averaging convolution filter of size $D \times D$;
 6. calculating a first bidimensional intrinsic mode function by subtraction of the mean envelope from the image;
 7. continuing repetition of steps 1–6 using the calculated smoothed mean envelope for the next empirical mode extraction
 8. stopping the whole process when the estimated disk diameter is too large (i.e. larger than half of the image).

The AFABEMD can be employed as a fringe pattern adaptive band-pass filter eliminating some part of the decomposition results (first BIMFs with high spatial frequencies correspond to higher harmonics and noise, whereas the several last modes are considered as fringe background). We apply the AFABEMD method both:

1. at the first step of Hilbert–Huang transform single-shot phase retrieval (fringe pattern pre-filtering removing first BIMF and several last ones according to the previously developed strategy [16]),
2. in a reference phase correction scheme (unwrapped HHT-retrieved phase distribution post-filtering).

3. The proposed modified variational image decomposition technique

Variational image decomposition is a relatively new method for background and noise removal from fringe patterns [22–25]. In this method the image is split into three components: the part containing background (structure), the one associated with fringes (texture), and noise. In this technique each of the decomposition components is modeled in a different function space and the result is obtained by minimization of designed functional. The choice of the appropriate function space and functional is an open issue which is constantly evolving to improve the decomposition capabilities.

Initially, VID was used to remove noise from images [28] and assumed image separation into structure (the main variability of the image) and texture (noise and small-scale repeated details). This way, high-frequency fringes would be qualified as noise. There are two approaches to overcome this problem: modeling the part associated with texture in different function spaces [29], or image separation into structure, texture and noise [30]. In the newest BV-G-shearlet model the parts associated with background, fringes and noise are modeled in the bounded variation (BV) space, the G space and the shearlet smoothness space, respectively. Minimization of the mentioned functionals is obtained using the orthogonal projection operator (BV and G space) [30, 31] and the shearlet shrink thresholding algorithm (shearlet smoothness space) [32]. The fringe image background may be considered

as a low-frequency component and can be modeled as structure in the VID algorithm. Fringes encoding optical phase are regarded as texture. It was shown that VID enables background and noise removal from fringes [22–25]. We will present a novel contribution corroborating the ability of VID to remove periodic error from the unwrapped phase distribution. Phase structure is automatically preserved with texture (residual fringes) and noise removed. In general, the calculation scheme for variational image decomposition can be described as:

- initialization: $noise(0) = texture(0) = structure(0) = 0$,
- main variational image decomposition loop:

$$\begin{aligned}
 \mathbf{noise}(n) &= \\
 & f - \mathbf{structure}(n-1) - \mathbf{texture}(n-1) \\
 & - SST(f - \mathbf{structure}(n-1) - \mathbf{texture}(n-1), \delta), \\
 \mathbf{texture}(n) &= \\
 & P_{G_\mu}(f - \mathbf{structure}(n-1) - \mathbf{noise}(n), N_1), \\
 \mathbf{structure}(n) &= \\
 & f - \mathbf{texture}(n) - \mathbf{noise}(n) \\
 & - P_{G_\lambda}(f - \mathbf{texture}(n) - \mathbf{noise}(n), N_2),
 \end{aligned}$$

- end of iterations: $n = N$,

where SST is shearlet shrink thresholding with a threshold δ , P_{G_μ} and P_{G_λ} are orthogonal projection operators with μ and λ coefficients, respectively, N is the number of main variational image decomposition iterations, and N_1 and N_2 denote the number of projection operator iterations for texture and structure estimation, respectively. At this stage of the algorithm's modification, we are focused only on finding the right number of orthogonal projection operators, because that has the greatest effect on the filtration result. The other parameters are responsible for ensuring the convergence of projection operator and energy distribution between decomposition components. Recommended values can be found in literature [30, 31] and their changing or adjusting is not a part of this work. As for the mentioned main variational image decomposition iterations, our experience shows that with properly defined projection operator iterations there is no need to repeat the calculations.

In the proposed modified variational image decomposition model, the parts connected with background and fringes are obtained using the orthogonal projection operator. In general, gradient-based methods are iterative, and we therefore expect to obtain a correct result after a specified number of algorithm steps. Furthermore, the result calculated in each consecutive step should be closer to the correct expected term rather than the one evaluated in the previous step, as long as convergence of the considered algorithm is preserved. In the first version of the variational image decomposition algorithm adapted to the fringe pattern filtration, the number of required steps of the projection operator was one of many parameters chosen by the user [22–25]. The task was not easy, and the suitable value of the mentioned parameter varies when analyzing different types of fringe patterns. Note that the problem of separation of closed fringes and the background described

by Gaussian function is quite different from the problem of separation of open fringes and the background described by a more complicated function. Our statement is connected with the image spatial frequency analysis. The second case is well-separated in the frequency domain, and fringes and background do not mix in the decomposition result. The Gaussian function and spherical phase function are similar and therefore difficult to distinguish. The need to automate the process of finding the right value of the parameter has naturally arisen.

Based on the mentioned property of gradient-based optimization methods, the authors propose a novel method for defining the end of the calculations. Instead of assuming the number of required projection operator steps, we calculate the difference between the results (x_n, x_{n+1}) retrieved in two consecutive steps $(\Delta, \text{equation (7)})$. To do that, we must define the representative value for the matrix, which can be the matrix norm. We decided to divide the obtained difference by the norm calculated from the initial image (f) to make the results independent of initial values, and to make the method itself robust and versatile $(\Delta_{norm}, \text{equation (8)})$. In addition, we noticed that what is more important for the retrieved VID result is how the mentioned difference is changing, rather than the difference value itself, so the derivative of the norm was calculated $(d\Delta, \text{equation (9)})$. In order to unify the estimated results for background and fringe parts, the derivative values are divided by the error obtained for the first two steps, and finally a tolerance parameter is proposed $(tol, \text{equation (10)})$.

$$\Delta = \|x_{n+1} - x_n\|_2, \tag{7}$$

$$\Delta_{norm} = \frac{\Delta}{\|f\|_2}, \tag{8}$$

$$d\Delta = abs\left(\frac{\Delta_{norm_{n+1}} - \Delta_{norm_n}}{2}\right), \tag{9}$$

$$tol = \frac{d\Delta}{\Delta_{norm_1}}. \tag{10}$$

Summing up, the number of projection operator steps is not chosen by the user; it is calculated automatically during decomposition by assuming the error value, which is more intuitive. In addition, the right error value is rather similar for all types of fringe patterns, which makes the proposed method versatile and robust to the fringe pattern origin.

The proposed tolerance parameter greatly facilitates and improves user work. To mark the importance of this fact, figure 2 presents a comparison of the image filtration results obtained by the standard VID model and its modified version. Two synthetic fringe patterns with high (figure 2(a)) and low (figure 2(b)) spatial frequency terms were simulated. The backgrounds to be separated were identical in the two fringe patterns. It is worth noting that if decomposition parameters are selected properly (the minimum root mean square error (RMS) point in the chart) the result given by VID does not differ from that given by mVID; see figures 2(c), (d) and (g), (h). On the other hand, if the parameter values are not chosen as optimal, which in this case means the same decomposition parameters for high and low frequency fringes (the green line

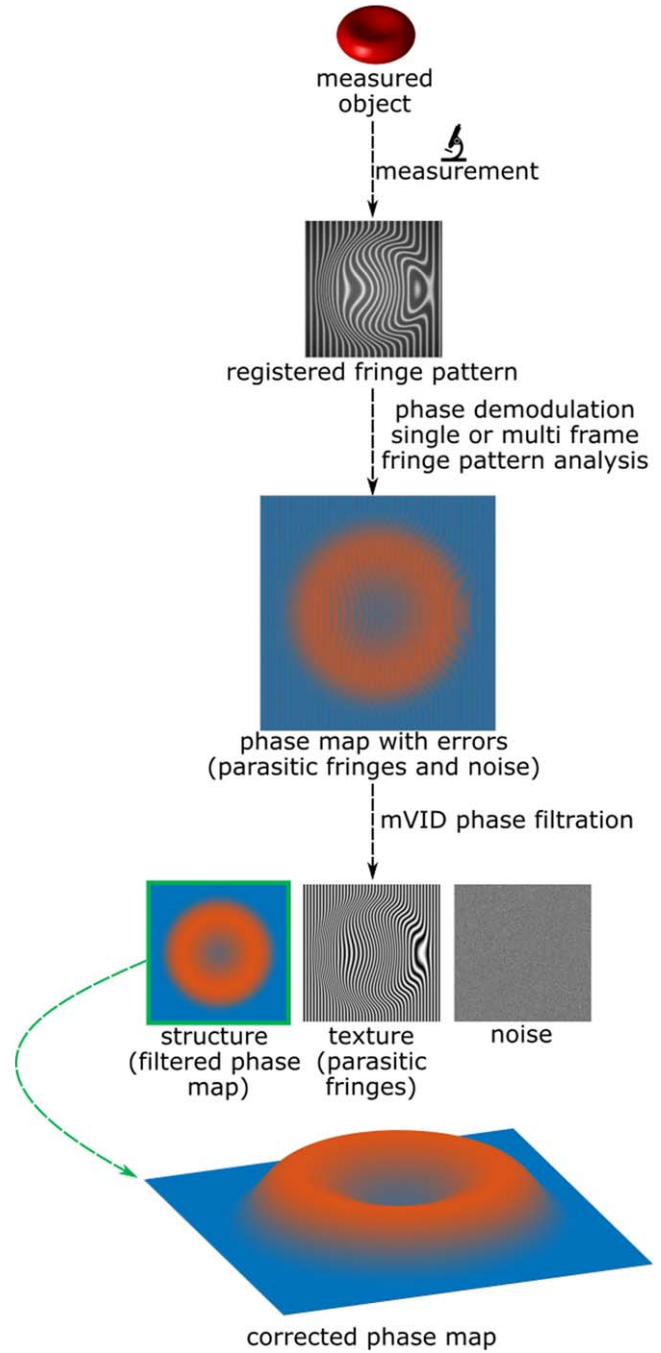


Figure 1. Scheme of the proposed phase enhancement approach.

on the chart), the obtained result can be far from what is expected. Conversely, the same error tolerance value set for different fringe patterns ensures correct results; for comparison, see figures 2(e), (f) and (i), (j). A decrease in carrier spatial frequency caused leakage of fringe information to the VID structure term (figure 2(e)), whereas mVID contained most of the fringe energy in the texture term. All single-frame fringe pattern processing methods are sensitive to the spatial frequency of fringes. Generally, the lower the spatial frequency of fringes is, the higher the errors introduced into the demodulated phase function are. Corroboration of this feature can be observed in figure 2.

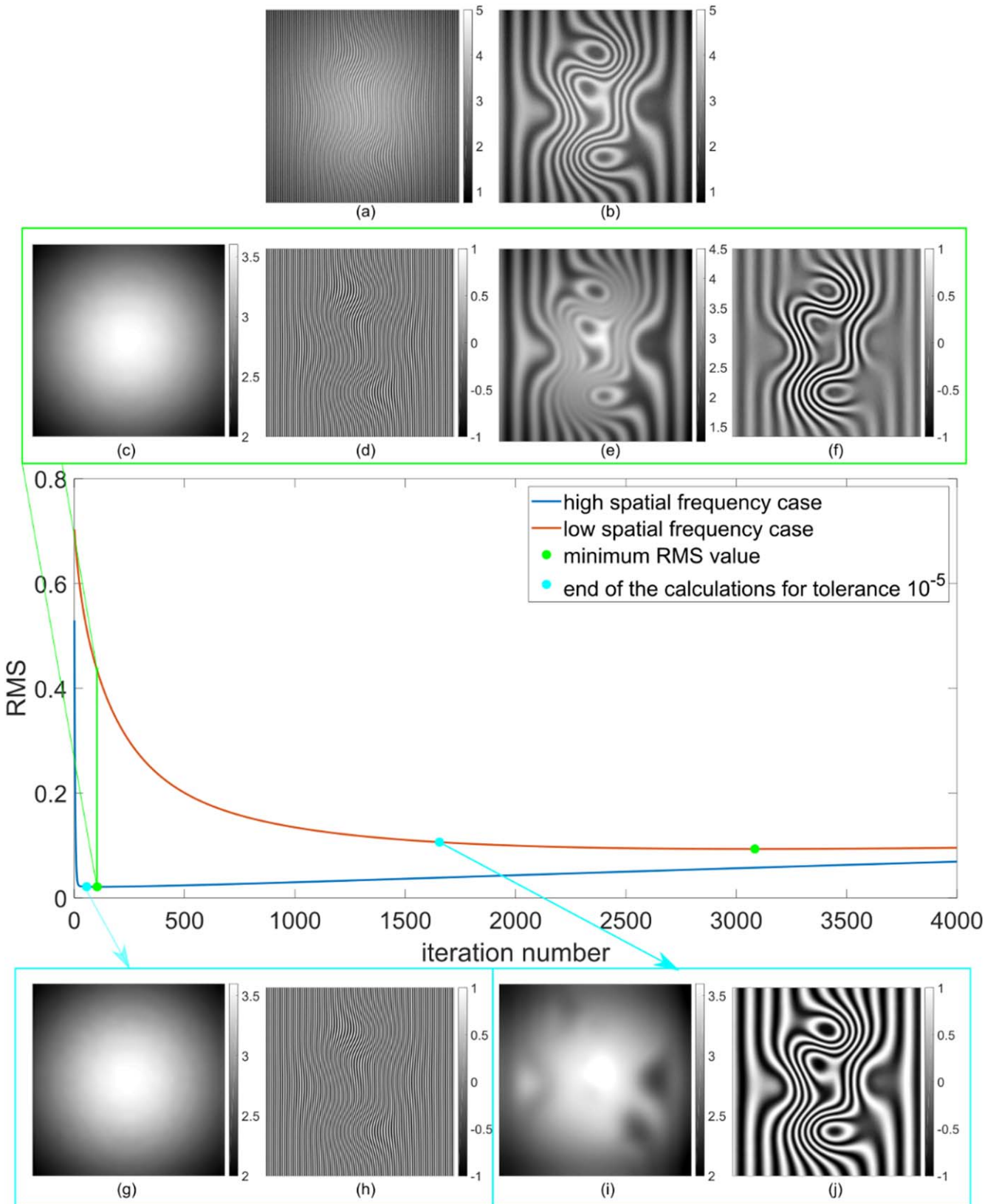


Figure 2. Comparison of results obtained by (c)–(f) VID and (g)–(j) mVID.

The calculation time needed to obtain fringe and background terms depends heavily on the number of projection operator iterations, which in turn depends on the assumed error tolerance value. The higher the error tolerance value, the

fewer iterations are needed. In general, we must perform more iterations when analyzing closed fringes than for open fringes. It is also worth mentioning that the shearlet shrink thresholding algorithm used to denoise the variational image

decomposition is time-consuming, in some cases even more so than the projection operator. The estimated time for a single projection iteration of a 512×512 fringe pattern is around 0.2 s on a standard PC, while noise estimation using the shearlet shrink thresholding [30, 32] takes 50 times longer (10 s). One should notice that finding the optimal number of iterations plays a key role in the decomposition process, not only because of the obtained result but also due to shortening the calculation time. It can be seen in the chart attached to figure 2 that with the use of the tolerance parameter in cases of both high and low frequency fringes, calculations ended before the RMS error reached its minimal possible value. Some readers may consider this a disadvantage of the proposed method. However, it should be noted that the difference between estimated RMS and minimal RMS is small ($2.22 \cdot 10^{-4}$ and 0.013 for high- and low-frequency fringes, respectively). At the same time we gained a computation time reduction, thanks to fewer iterations. In order to increase the accuracy of the retrieved result, we encourage lowering the tolerance value at the expense of calculation elongation. It should also be noted that with too many iterations, the RMS value increases due to low-frequency background leakage to the extracted part of fringes.

4. Numerical simulations

To study the proposed mVID approach, a synthetic fringe pattern was numerically generated with a carrier peaks phase function, uneven background, noise, and nonlinearities. It is presented in figure 3(a). For simulations, we used a Matlab computational environment. The synthetic interferogram can be described as:

$$I(x, y) = a(x, y) + \cos\left(\varphi + \frac{2\pi}{T}x\right) + n_{std} \cdot randn(512), \quad (11)$$

in the case of open fringes, and:

$$I(x, y) = a(x, y) + \cos(\varphi) + n_{std} \cdot randn(512), \quad (12)$$

in the case of closed fringes. In both equations x, y denote image coordinates simulated with the use of Matlab function *meshgrid(1:512)* for open fringes and *meshgrid(linspace(-pi, pi, 512))* for closed fringes, while $a(x, y)$ denotes background simulated as a Gauss function, φ denotes phase function simulated here as a Matlab 'peaks' function for open fringes and spherical function ($\varphi = z \cdot (x^2 + y^2)$) relates to closed fringes, T denotes the period of carrier fringes, n_{std} denotes the standard deviation of the noise, and *randn(512)* is a Matlab function, which enables us to simulate normally distributed pseudo-random numbers.

To recall the proposed calculation path, the first step is fringe pattern filtering with the use of the AFABEMD algorithm, and the second step is connected with estimating the phase function with the use of the spiral Hilbert transform.

Both steps form a HHT. Figure 3(b) presents the phase distribution demodulated using the HHT and figure 3(c) depicts the overall phase demodulation error calculated by subtracting the simulated ground truth phase map from the retrieved one. One can clearly note the influence of noise and residual fringes originating from the fringe non-cosinusoidal (non-linear) profile and non-zero background term. Fringe pattern pre-filtering (the first part of the HHT) encompasses the AFABEMD decomposition and automatic noise removal and background rejection using the scheme reported in [16, 33]. The background, fringe, and noise components derived from the synthetic fringe pattern using the AFABEMD algorithm are depicted in figures 3(d)–(f), respectively.

The third step of the proposed calculation path is connected with demodulated phase enhancement. Undesired artifacts were removed using the proposed AFABEMD and mVID techniques. The AFABEMD method consists in the unwrapped phase map decomposition of a set of empirical modes and automatic residual smoothed phase term extraction, i.e. the last M decomposition components are added. The number M is determined using the condition that $M + 1$ added terms create a filtered phase with a higher root mean square (RMS) error than M modes. An exemplifying decomposition of the erroneous HHT-retrieved phase, which can be seen in figure 3(b), is presented in figures 4(b)–(k), whereas figure 4(a) shows the error map of HHT-retrieved phase distribution corrected using the AFABEMD scheme. The filtered phase was calculated by summing all modes with numbers higher than 2 ($M = 9$, green frame). The so-called mode mixing phenomenon is observed in figure 4; a single component travels across several modes (figures 4(g)–(k)) and a single mode stores different components (figure 4(d)). Removing the first two modes is treated as a default strategy for AFABEMD phase enhancement.

The VID algorithm simply calculates the phase structure. The straightforward nature of this approach is clearly advantageous at this point. Three mVID components of the HHT demodulated phase distribution are depicted in figures 4(l)–(n) with filtered phase (mVID structure) in figure 4(l), residual fringes (mVID texture) in figure 4(m), and noise in figure 4(n). Figure 4(o) presents the phase error map after VID correction (preserving structure). Comparing the error maps retrieved by the HHT-AFABEMD and HHT-mVID methods, it is noticeable that the first one could not separate residual fringes and true phase successfully. This is connected with the mode mixing problem; more residual fringes removed implies more phase details filtered incorrectly. One can consider the fact that this issue could be also present in the case of mVID correction. Too many Chambolle projection algorithm iterations can cause leakage of phase details to the residual fringes part in the same way as was mentioned regarding fringe pattern filtration (background leakage to the fringes part). However, as was shown in section 3, tolerance value manipulation enables changing the end point of calculations and therefore the filtration result can be adjusted to user expectations.

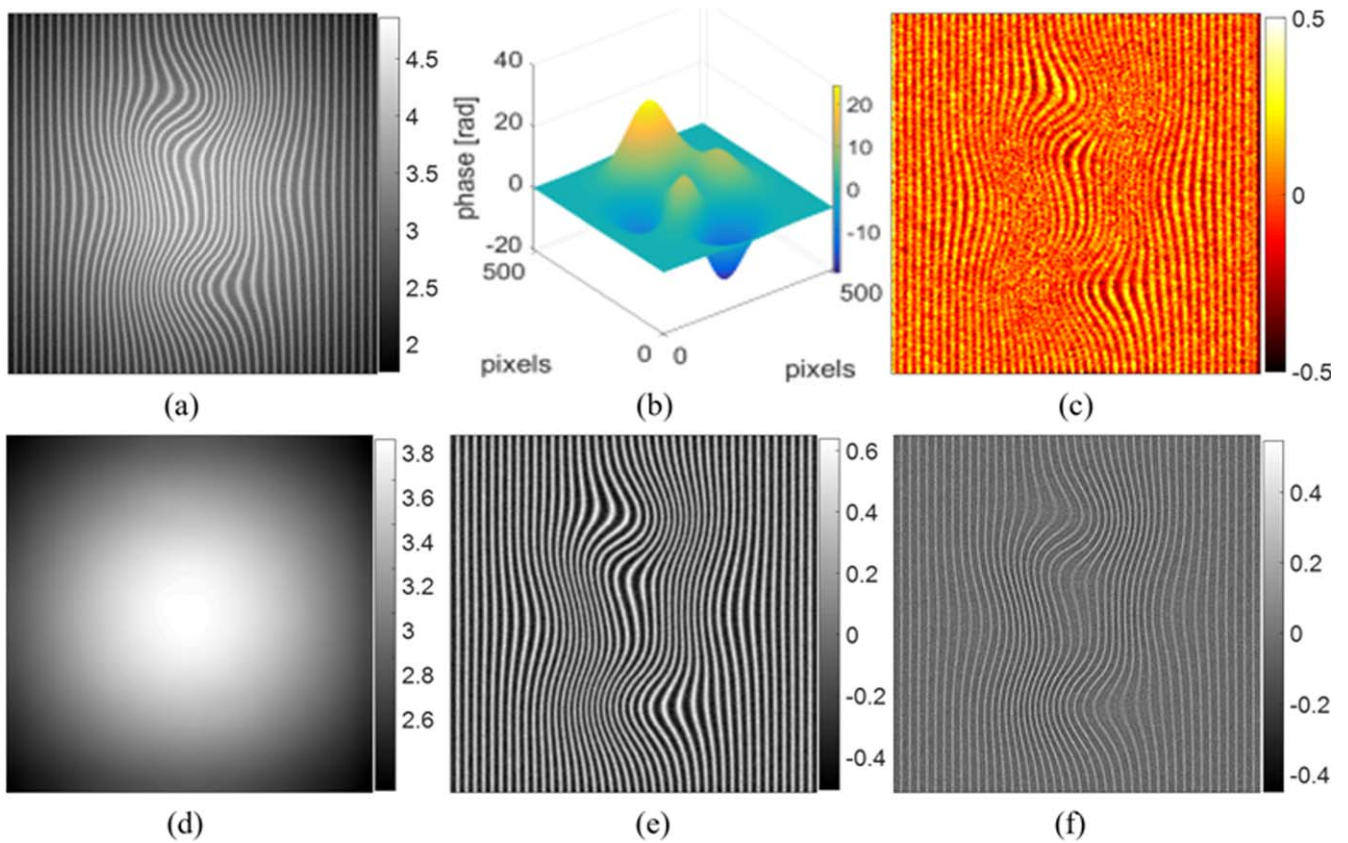


Figure 3. Synthetic carrier fringe pattern processing. (a) Simulated fringe pattern, (b) its phase distribution (with linear term removed) demodulated using the HHT method, (c) phase error map calculated as a difference between HHT-retrieved phase and ground truth simulated phase function, (d) fringe pattern background term, (e) fringe term, and (f) the noise part filtered using the AFABEMD method.

The cross-sections through phase correction results presented in figure 5 show successful phase error reduction by the examined AFABEMD and mVID techniques. However, their slight tendency to fringe local shape variation is visible. (The main error areas are located around the phase function extrema, which is symptomatic of single-frame demodulation.) The underlying phase function should be smooth, i.e. as encountered in real optical component testing (lenses, etc). The first of the analyzed phase distributions was encoded in high-frequency open fringes, which is connected with easier filtration in both the image and phase domains. Therefore, the value of error tolerance for the mVID algorithm might be higher than usual, which is related to the iteration number reduction. In this case, there are no visible border effects. The separation of concentric parasitic fringes and spherical phase function is definitely a more difficult issue. The error tolerance value must be more stringent and we can observe clear border effects, as shown in figure 5(b).

Next, a comprehensive analysis of isolated error sources was conducted. We studied the influence of nonlinearities, noise, background, and fringe spatial frequency on the studied AFABEMD and mVID phase correction efficiency. The regular VID method was not examined since it was already studied in the literature [22–25] and we proved the advantage of mVID in the previous section. Each studied case concerned

a single separated error source and two phase functions, i.e. the carrier peaks phase function and spherical function, thus making our evaluation sensitive to differences in overall phase function shape. For each case, the plot representing the studied relations is provided alongside the exemplifying fringe patterns and their uncorrected or corrected phase error maps.

4.1. Error source analysis: fringe nonlinearity

Figure 6 presents the relation between the nonlinear gamma (γ) parameter describing the fringe nonsinusoidal profile deviation and RMS for the obtained phase distributions. The curves relating to the AFABEMD filtration method show a similar trend to those for no filtration case, while the mVID filtration method seems to be more stable and accurate. The influence of nonlinearity on fringe pattern intensity can be described as:

$$I'(x, y) = I(x, y)^\gamma, \quad (13)$$

where $I'(x, y)$ denotes output and $I(x, y)$ denotes input intensity. The increase of error value around $\gamma = 1$ (linear case) after phase filtration is worth mentioning. It is easy to explain in the case of mVID filtration that it is due to the decomposition nature. Unnatural ‘true’ phase decomposition into three components results in the loss of data. In order to

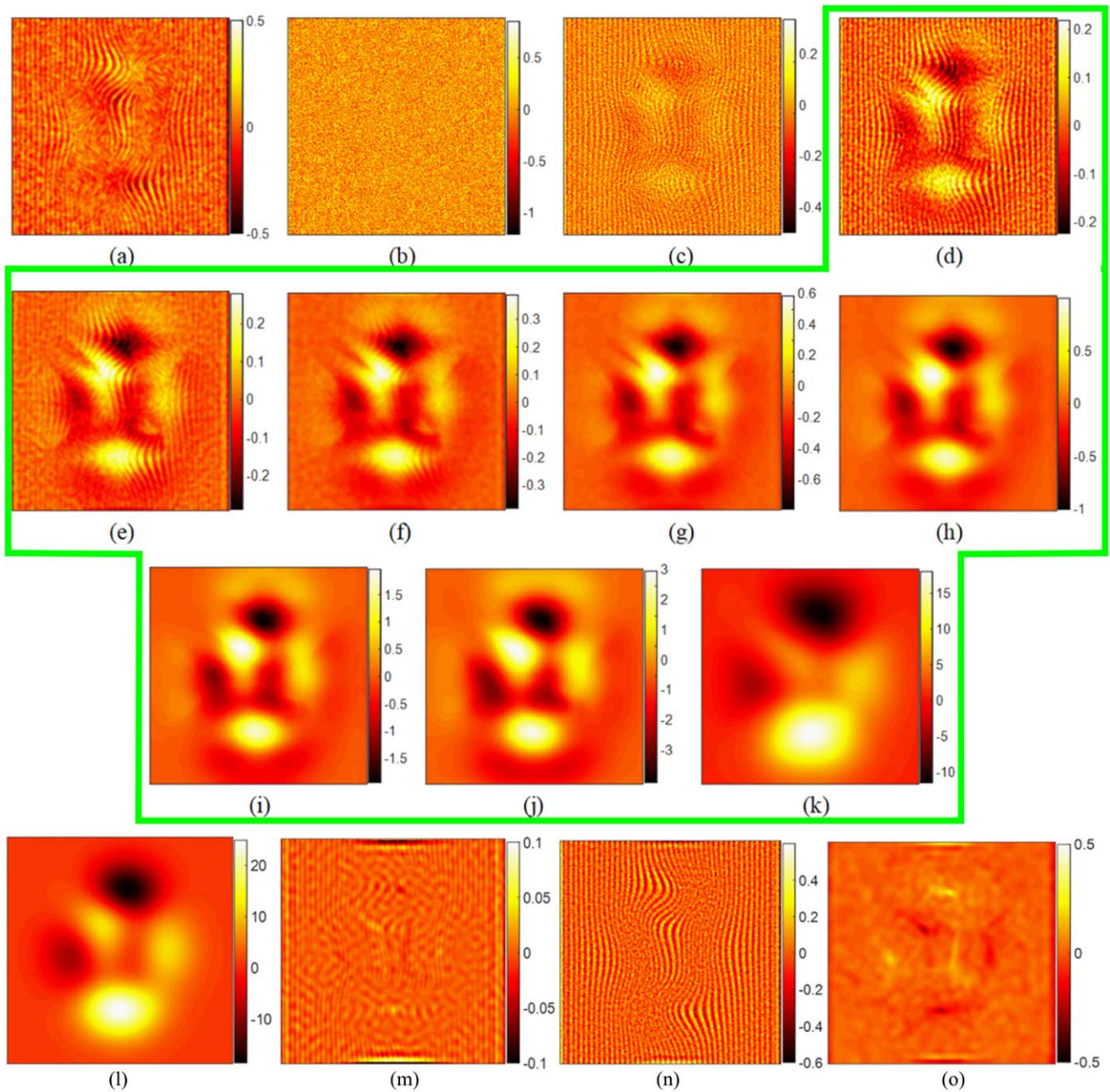


Figure 4. Correction of error in demodulated phase using the AFABEMD method. (a) The error map of HHT-retrieved phase distribution corrected using the AFABEMD scheme. (b)–(k) Ten modes representing the full AFABEMD decomposition of the HHT-retrieved phase. Three mVID components of the HHT demodulated phase distribution: (l) filtered phase estimated as VID structure term, (m) residual fringes estimated as mVID texture term (m) and (n) noise; (o) phase error map after VID correction implemented by preserving structure term. Values are in radians.

start the decomposition process for the AFABEMD algorithm, white Gaussian noise with a low standard deviation was added to the rather smooth phase function. In the $\gamma = 1$ case, this action also causes loss of data.

4.2. Error source analysis: fringe pattern noise

Figure 7 shows the relationship between the standard deviation of noise and RMS phase error. The noticeable increase in RMS

value in the case of an unfiltered phase arises due to the suggested noise removal method (strong noise is present in a higher number of modes). Nonetheless, the proposed phase filtration algorithms can minimize not only errors resulting from nonlinearities but also from inappropriate fringe pattern pre-filtration. One should always keep in mind that strong, unfiltered noise can make phase retrieval difficult or even impossible. For weaker noise, the dominant source of error is nonlinearity, but with increasing standard deviation the noise takes the lead.

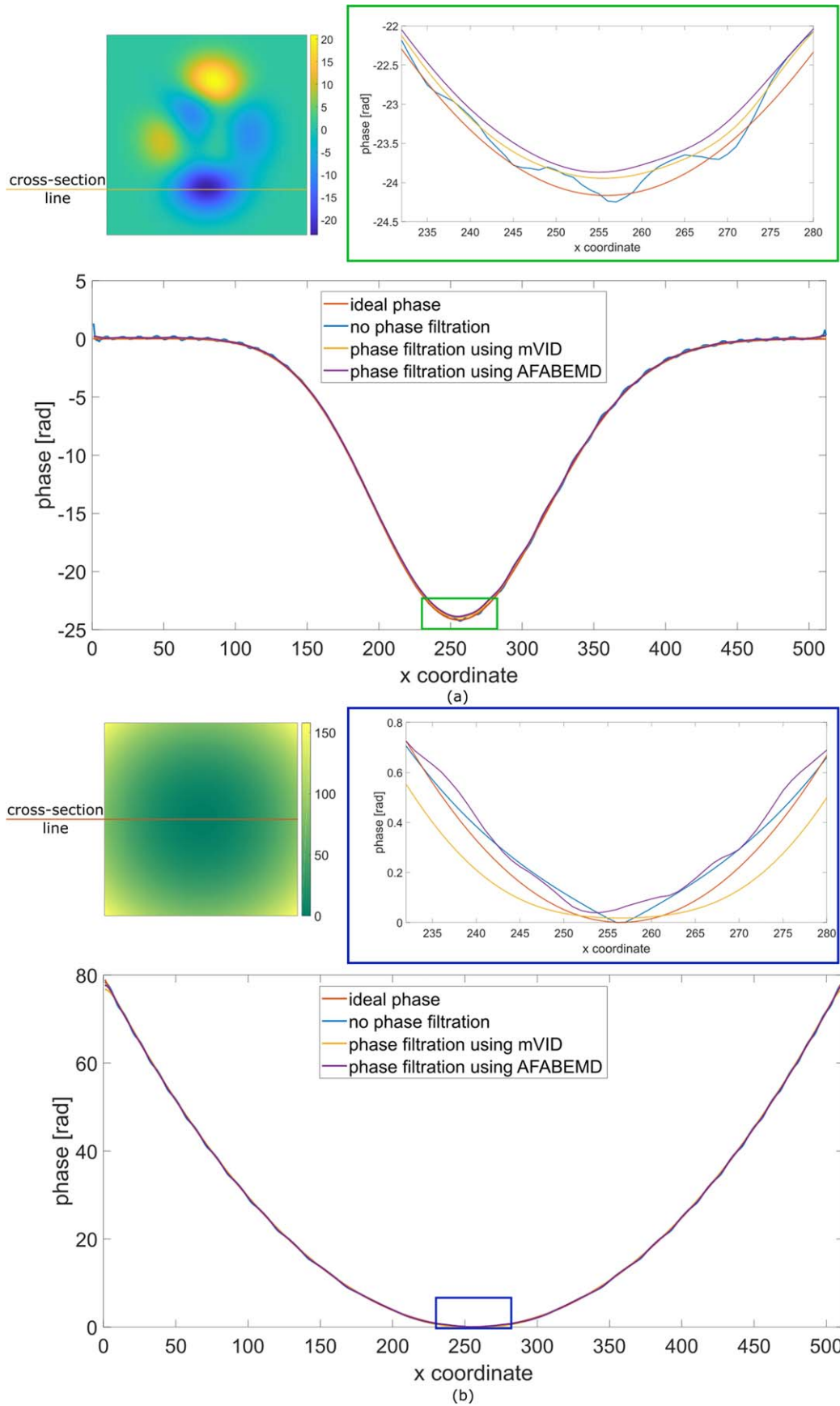


Figure 5. Cross-section of the phase function for (a) open fringes (peaks phase function, carrier fringes period 12 px) (note: higher tolerance for mVID, lower border effects), and (b) closed fringes (spherical phase function).

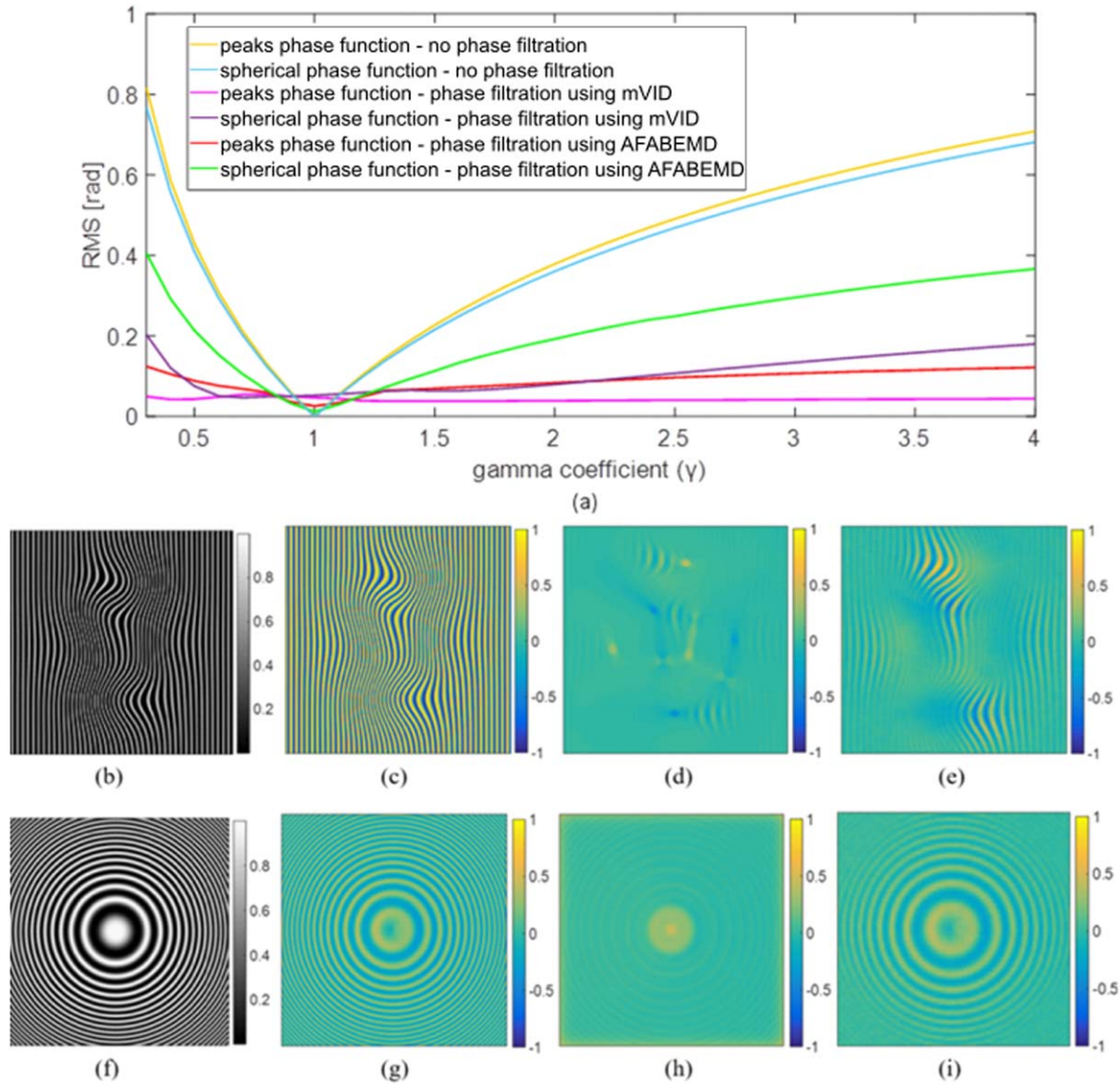


Figure 6. Influence of nonlinearities: (a) relation between nonlinear gamma parameter describing the fringe profile deviation and RMS for the obtained phase distributions; (b), (f) analyzed fringe patterns ($\gamma = 1,5$) with open and closed fringes, respectively; (c), (g) phase error before filtration; (d), (h) phase error after mVID filtration; (e), (i) phase error after AFABEMD filtration.

4.3. Error source analysis: fringe pattern background illumination

A simulated fringe pattern with variable background intensity can be described as:

$$I(x, y) = ka(x, y) + b(x, y)\cos(\text{phase}(x, y)). \quad (14)$$

Figure 8 describes the relation between final phase RMS errors and magnitude (k) of the added background (k times) described by Gaussian function (the peaks function was also studied, with a very similar outcome); see equation (9). The RMS values for low and high intensity backgrounds (low and high values of k , respectively) are similar, which shows that the suggested background removal method is accurate and stable over a wide range. Again the mVID correction is the best, with one noticeable unintuitive feature, i.e. the error decreases with the increase of the background magnitude for

spherical fringes. Once again the largest errors are observed around phase function extrema.

4.4. Error source analysis: fringe spatial frequency

Figure 9 depicts the RMS error curves for different spatial frequencies of fringe patterns with the same imperfections (noise and background levels). The mode mixing problem causes the increase of RMS value for high-frequency fringes in cases of an unfiltered phase. To be exact, the noise cannot be removed from the fringe pattern without removing high-frequency fringes (present in BIMF1) in the process. Hence, the first BIMFs must be preserved with all high-frequency noise. Although noise freely transfers from intensity into phase domain, our phase filtration algorithms can minimize noise-related errors successfully. Single-frame fringe analysis techniques generally cope better with high-frequency fringes, hence the increase of phase demodulation errors with the

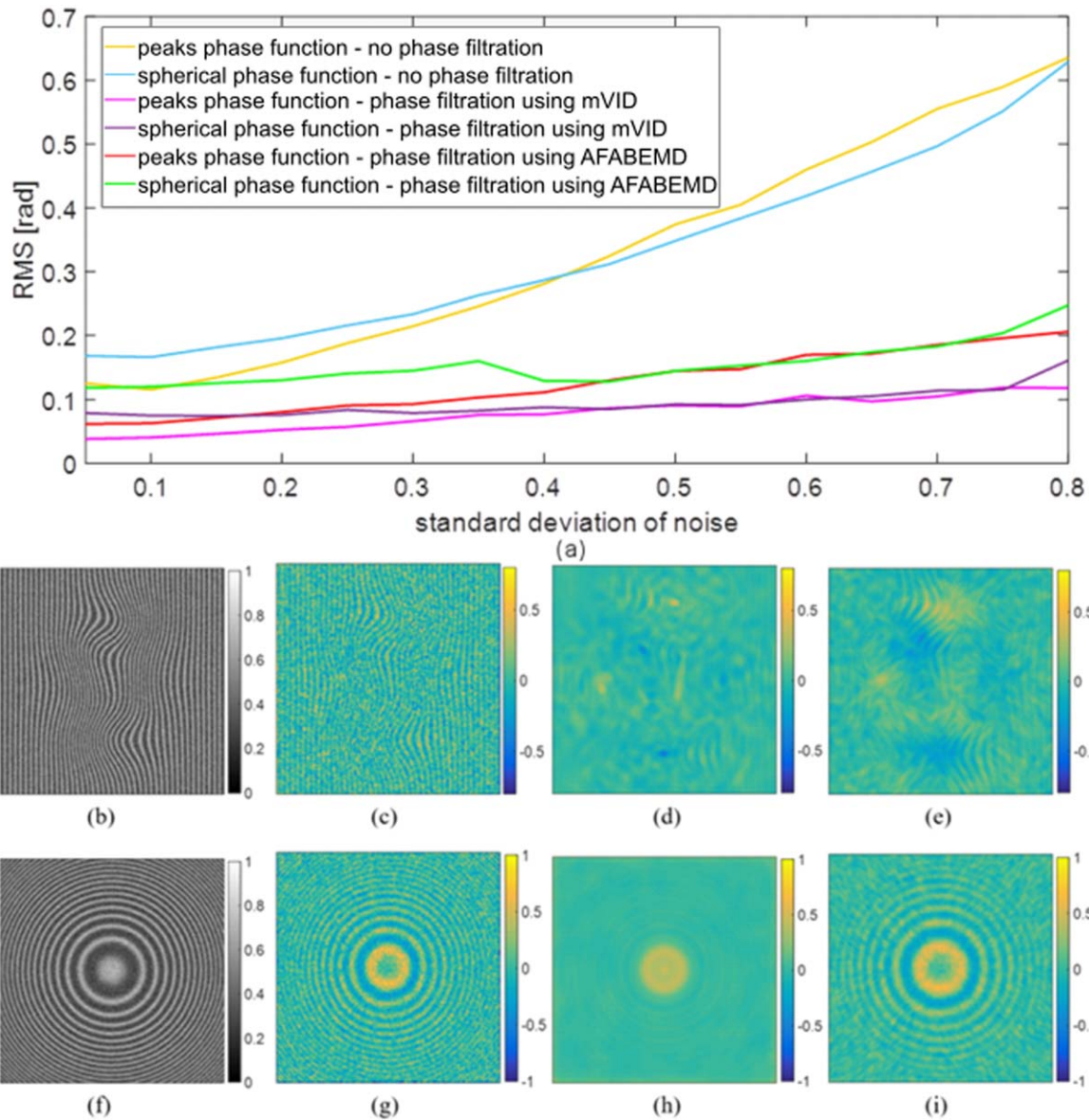


Figure 7. Influence of noise ($\gamma = 2$): (a) relationship between standard deviation of noise and RMS phase error; (b), (f) analyzed fringe patterns with open and closed fringes, respectively (standard deviation of noise 0.2); (c), (g) phase error before filtration; (d), (h) phase error after mVID filtration; (e), (i) phase error after AFABEMD filtration.

increase of fringe period (spatial frequency decrease). In both presented cases, the influence of the noise was overcome; see figures 9(c) and 8(e). Improperly filtered noise in an image domain is a much simpler problem, even if it transfers into a phase domain, than the problem of parasitic fringes.

5. Experimental validation

For primary experimental verification, a set of five $\pi/2$ phase-shifted interferograms of silicon rectangular micromembranes was taken in a Twyman–Green type of interferometric microelectromechanical systems (MEMS) test station as described in [34]. A reference ground-truth phase corresponding to the membrane shape was calculated using the principal component analysis phase-shifting algorithm [35],

unwrapped, and denoised using a Gaussian kernel (31×31 px, $\sigma = 5$). It is presented in radians in figure 10(a). A non-linear interferogram modified in Matlab by setting the gamma parameter of the correctly recorded frame to be equal to 2 is shown in figure 10(b) (initially it was equal to 1). The error map of the single-frame HHT-demodulated phase distribution is depicted in figure 10(c). Phase error maps after AFABEMD and mVID corrections are presented in figures 10(d) and (e). RMS values decreased from 0.37 radians to 0.05 (AFABEMD) and 0.07 (mVID), which is a very good result. The visible electrode pattern in the case of mVID filtration error confirms its detail preservation feature.

The second experimentally recorded fringe pattern, figure 11(a), stores information about the refractive index structure characterizing healthy prostate cells (RWPE-1). The given interferogram is representative of one of the most

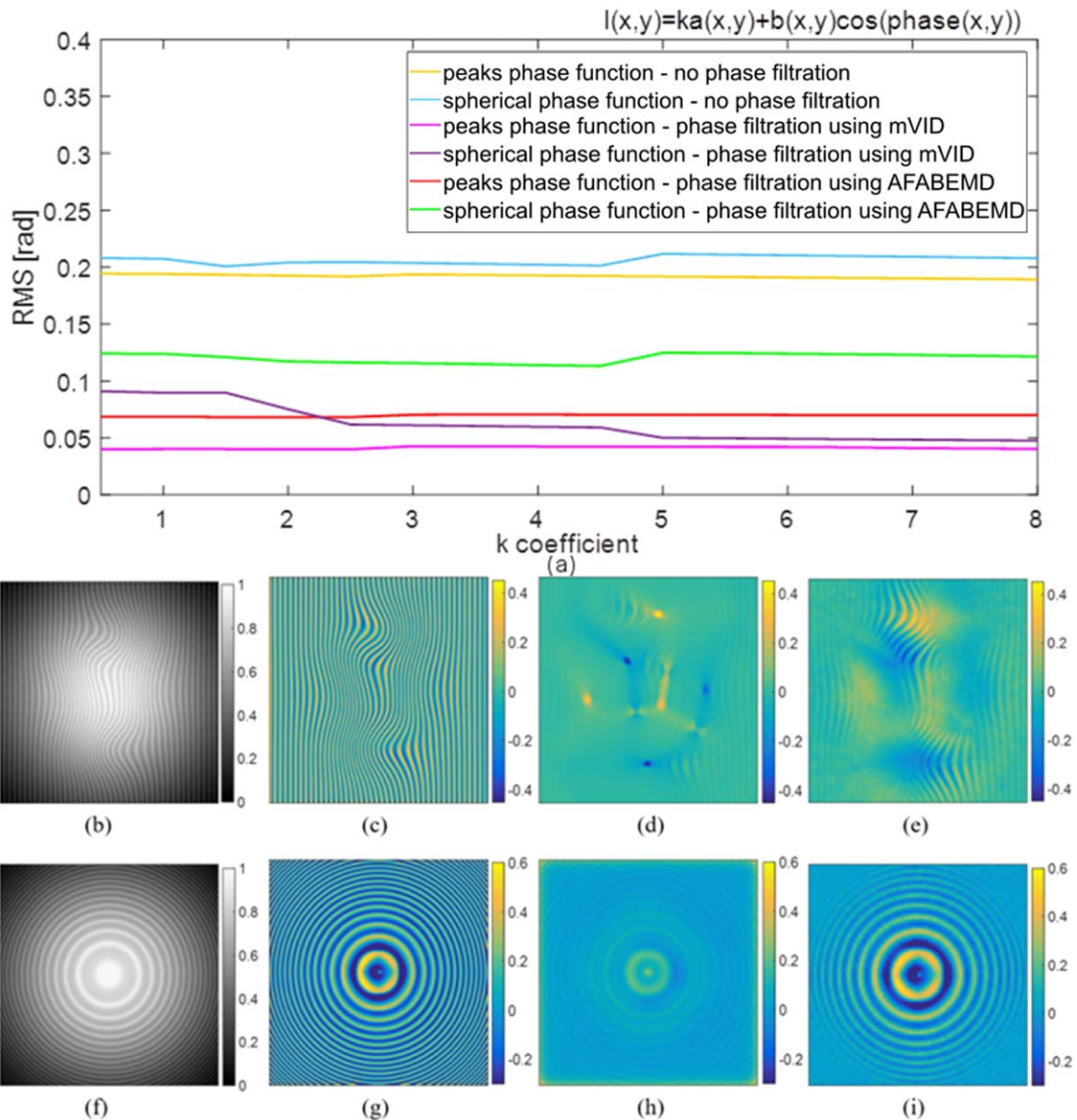


Figure 8. Influence of background ($\gamma = 2$): (a) relation between final phase RMS errors and magnitude of the added background described by Gaussian function; (b), (f) analyzed fringe patterns with open and closed fringes, respectively ($k = 8$); (c), (g) phase error before filtration; (d), (h) phase error after mVID filtration; (e), (i) phase error after AFABEMD filtration.

popular and fastest-developing methods in biomedical full-field optical metrology, i.e. quantitative phase imaging [36–38] (QPI). In QPI the measurement is usually achieved by interference, e.g. digital holographic microscopy or interference microscopy. In the case of figure 11, a spatially multiplexed interference microscope described in [38] was used to record the fringe pattern. The HHT-retrieved phase function can be seen in figure 11(b). The clearly visible noise is the result of an inability to distinguish noise and fringes in interferogram pre-filtering (high-frequency fringes and noise stored together in the first BIMF). However, it can be clearly seen that both mVID (figures 11(c) and (d)) and AFABEMD (figures 11(e) and (f)) compensate for the mentioned phase errors. It is worth noting that parasitic interference fringes were also removed

successfully. The mVID can be seen as advantageous in terms of detail preservation while the AFABEMD method employs more significant smoothing.

The last interferogram (figure 12(a)) analyzed using the proposed calculation path was registered with the use of the electronic speckle pattern interferometry setup described in [39]. The fringe pattern presents correlation fringes encoding information about in-plane displacements of the cantilever beam mounted on the left side and loaded at the opposite end. The result of HHT can be seen in figure 12(b). One can notice that the retrieved phase map is smooth (slowly varying) but noisy and with discontinuities. Considering that, it is a great candidate for testing the proposed phase enhancement method. The filtration result (the structure part of the mVID

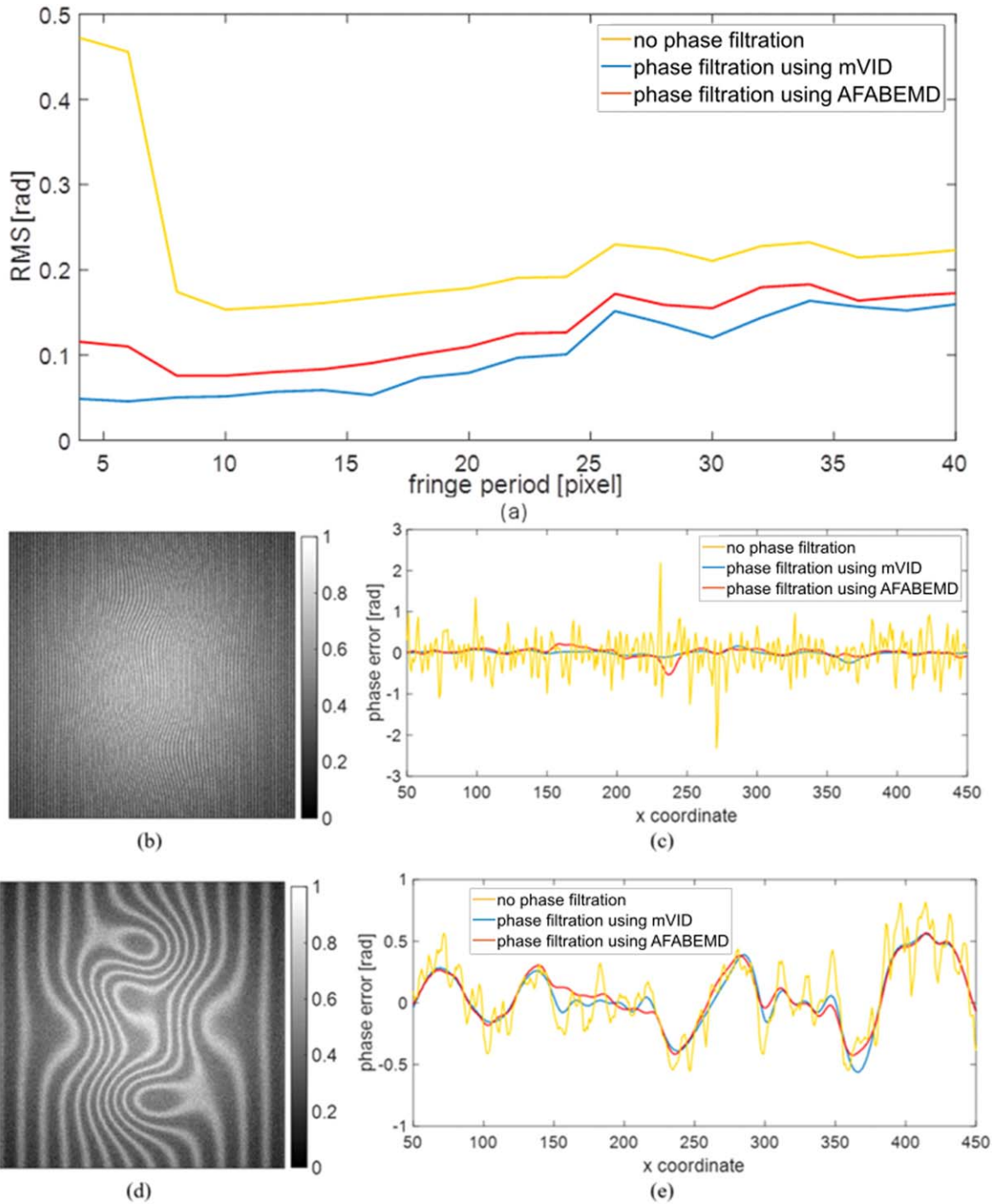


Figure 9. Influence of the fringe spatial frequency ($\gamma = 2$): (a) relation between final phase RMS errors and the fringe spatial frequency, (b) analyzed fringe pattern with period of carrier fringes equal to six pixels, (d) period of carrier fringes 40 pixels; (c), (e) cross-section of estimated errors.

decomposition) is presented in figure 12(c), and the neglected part (the texture and noise parts of the mVID decomposition) is presented in figure 12(d). For comparison, the AFABEMD results are presented in figures 12(e) and (f). It is worth noting that in the texture and noise part (figure 12(d)), no phase details are visible but only nonlinearities corrupted the result after previous calculations. In the case of AFABEMD filtration, some of the phase information was removed incorrectly.

6. Closing remarks and perspectives

We would like to sum up and emphasize the novel contributions presented in the manuscript.

1. A novel methodology for phase error removal based on the empirical and variational image decomposition. For the first time, both techniques were used for phase error

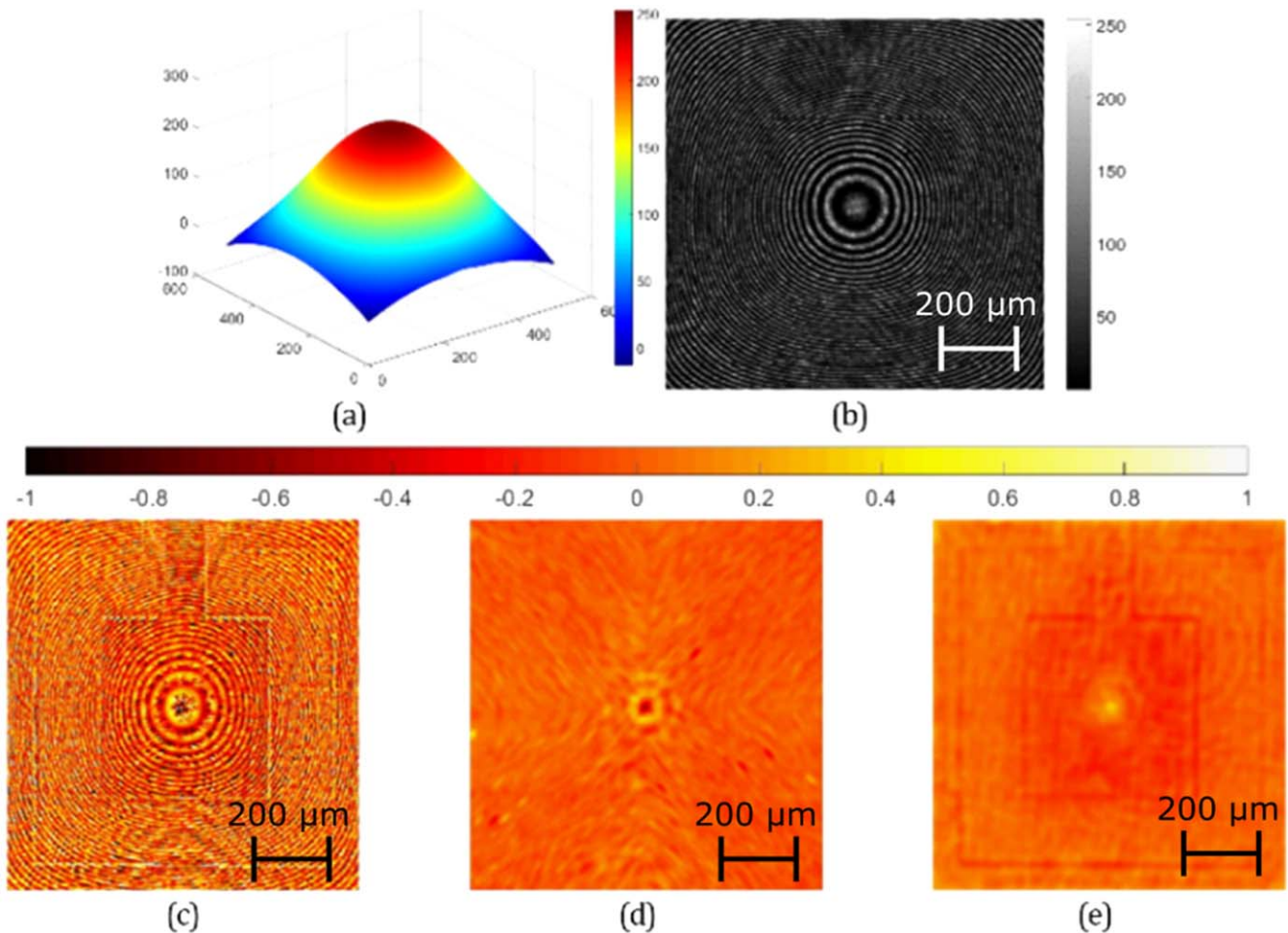


Figure 10. Experimental evaluation of the shape of active silicon micromembrane [34]; (a) referenced ground-truth phase function calculated by the principal component analysis phase-shifting algorithm; (b) interferogram with introduced nonlinearity, and; error maps (c) for single-frame HHT-demodulated phase distribution and (d) after AFABEMD correction and (e) after mVID correction.

reduction. The proposed concept differs significantly from the fringe pattern intensity domain processing. Fringe filtering enables the recovery and preservation of the image term associated with a fringe oscillatory component (discarding the low-frequency background and high-frequency noise), whereas in phase domain filtering we aim to eliminate the parasitic oscillatory component (parasitic residual fringe pattern) present due to uneven background and nonlinearity errors (fringe filtering and phase demodulation imperfections). In this way we propose a novel, robust loop for fringe filtering and phase refinement based on especially tailored modified empirical and variational image decomposition. It is insightful to realize that the same techniques, with slight but crucially efficient modifications, can serve the purpose of error reduction in both fringe intensity domain and phase domain. Comprehensive yet straightforward double-domain filtering provides enhanced measurand recovery (such as the shape of the micromembrane), i.e. the task of fringe pattern based optical full-field measurement techniques (such as interferometry, structured illumination, moiré methods, holography and quantitative phase imaging [36–38]), where the impact of this work is focused.

2. A novel, modified variational image decomposition (mVID) method with unique properties and significant advancements over regular VID:
 - 2.1 Automation, so there is no need for time-consuming blind parameter (number of iterations) estimation. The proposed decomposition tolerance solution determines when variational decomposition is finished, and it stops automatically after reaching the pre-assumed tolerance threshold.
 - 2.2 Versatility introduced by a normalized tolerance parameter set to 10^{-5} . The proposed value should provide successful decomposition for different kinds of fringe patterns (closed fringes, open fringes, strong Gaussian background, etc). We have used this value throughout the paper.
3. Detailed studies of the proposed mVID technique using a numerically simulated environment and real-life experiments corroborating its effectiveness and thoroughly evaluating advantages over the reference method and limitations.

From the viewpoint of execution time, the AFABEMD algorithm is the more attractive. The mVID image classification

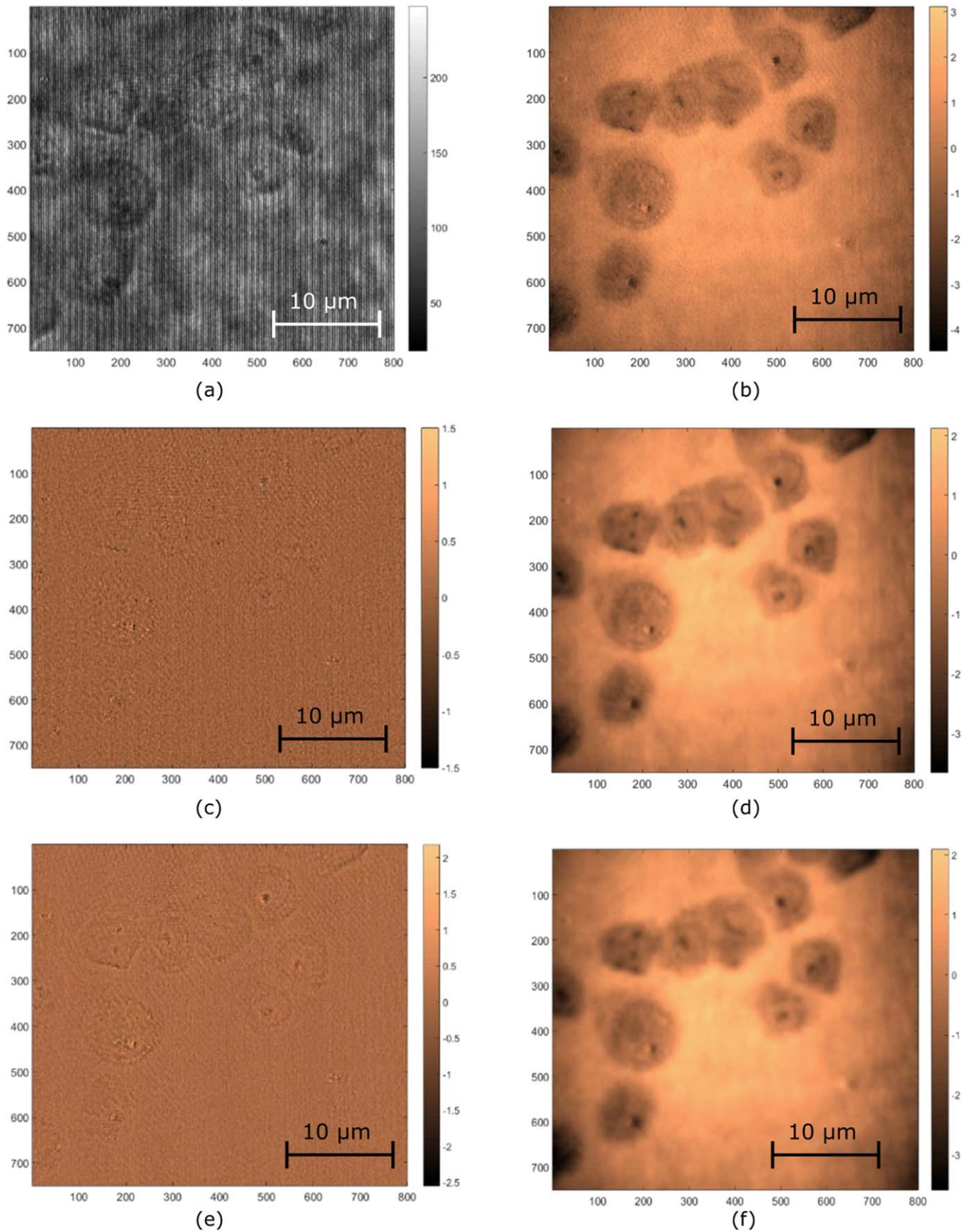


Figure 11. Healthy prostate cells analysis. (a) Registered interferogram; (b) HHT-retrieved phase function; (c) phase error removed using mVID (texture + noise decomposition components); (d) corrected phase function by mVID; (e) phase error removed using AFABEMD, and; (f) corrected phase function by AFABEMD.

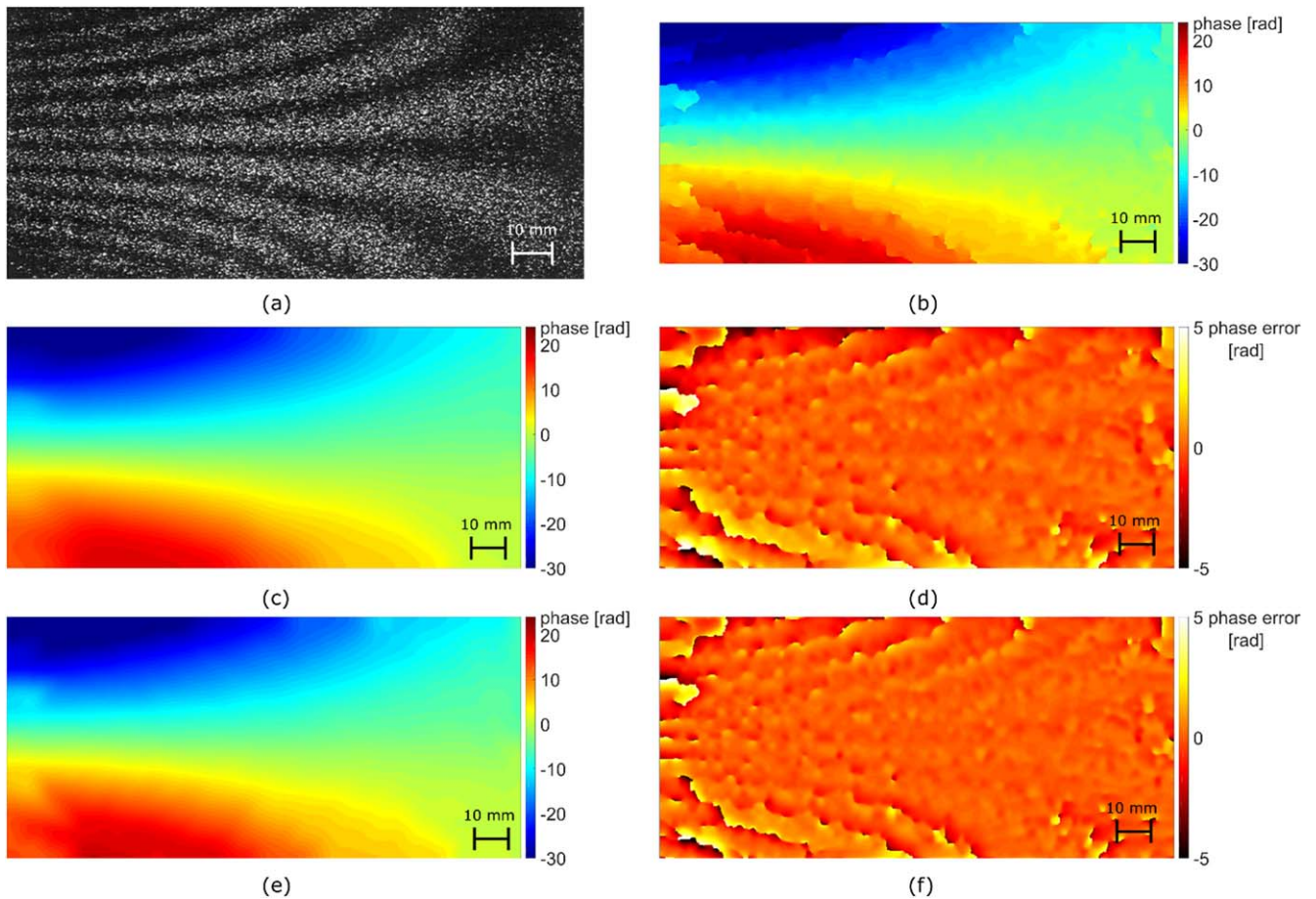


Figure 12. Cantilever beam in-plane displacement measurement [39]. (a) Registered interferogram; (b) HHT-retrieved phase function; (c) corrected phase function by mVID; (d) phase error removed using mVID (texture + noise decomposition components); (e) corrected phase function by AFABEMD, and; (f) phase error removed using AFABEMD.

takes several minutes, whereas AFABEMD (optimally implemented using mathematical morphology) can automatically filter the same 512×512 px image in around one second. The mVID method has the advantage of straightforwardly organizing a fringe pattern into a noise, fringe, and background parts. Conversely, the AFABEMD requires an automatic modes allocation strategy if it is to perform well. It is important to emphasize that AFABEMD decomposition needs extrema in the image in order to extract well-scaled and meaningful modes. In cases of successful pre-filtering, the unwrapped phase function can contain fringe-like errors smooth enough to be extrema-less. In this case, it is crucial to add white noise with very low variance to seed extrema artificially and provide a valid base for meaningful AFABEMD decomposition. Another sound approach assumes no denoising in fringe pattern pre-filtering (only background removal, for efficient HHT operation). This concept can be employed until the noise level is too heavy for phase unwrapping. The VID is free of such limitations, and additionally exhibits better detail preservation. The VID-enhanced experimental phase error contains a characteristic electrode pattern (active silicon micromembrane studies) whereas AFABEMD removed it successfully; see figure 10. The phase correction

scheme presented in this contribution combined with AFABEMD pre-filtering and 2D Hilbert phase demodulation can be seen as a complete solution for full single-shot fringe processing and analysis path.

In future studies, we will focus on developing efficient extrapolation schemes to avoid the border effect problem. In this paper, we assumed that we have a perfect extrapolation procedure, simulating or recording images and taking into account their central regions. One can also imagine an experiment where interesting fringes are contained in the center of the field of view.

Acknowledgments

We acknowledge the support of Faculty of Mechatronics Warsaw University of Technology statutory funds and Dean's grant. The experimental work [34] from which the data presented in figure 10(b) were taken was co-supported by the European Union (EU) Project OCMMM (in part in the Laboratoire d'Optique P.M. Duffieux, Université de Franche-Comté, Besançon, France).

Funding

National Science Center, Poland (OPUS 13 2017/25/B/ST7/02049), WUT statutory funds, Polish National Agency for Academic Exchange, National Natural Science Foundation of China (61722506, 61505081).

ORCID iDs

Maria Cywińska  <https://orcid.org/0000-0001-6246-2727>

Maciej Trusiak  <https://orcid.org/0000-0002-5907-0105>

References

- [1] Servin M, Quiroga J A and Padilla M 2014 *Fringe Pattern Analysis for Optical Metrology: Theory, Algorithms, and Applications* (New York: Wiley)
- [2] Schwider J 1990 Advanced evaluation techniques in interferometry *Progress in Optics* ed E Wolf (Amsterdam: Elsevier)
- [3] Malacara D 2007 *Optical Shop Testing* 3rd edn (New York: Wiley)
- [4] Takeda M, Ina H and Kobayashi S 1982 Fourier-transform method of fringe-pattern analysis for computer-based topography and interferometry *J. Opt. Soc. Am.* **72** 156–60
- [5] Kemaq Q 2013 *Windowed Fringe Pattern Analysis* (Bellingham, WA: SPIE)
- [6] Zhong M, Chen W and Jiang M 2012 Application of S-transform profilometry in eliminating nonlinearity in fringe pattern *Appl. Opt.* **51** 577–87
- [7] Pokorski K and Patorski K 2013 Processing and phase analysis of fringe patterns with contrast reversals *Opt. Express* **21** 22596–609
- [8] Li B, Tang C, Zhu X and Xu W 2016 Shearlet transform for phase extraction in fringe projection profilometry with edges discontinuity *Opt. Lasers Eng.* **78** 91–8
- [9] Pirga M and Kujawinska M 1995 Two directional spatial-carrier phase-shifting method for analysis of crossed and closed fringe patterns *Opt. Eng.* **34** 2459–66
- [10] Kai L and Kemaq Q 2013 Improved generalized regularized phase tracker for demodulation of a single fringe pattern *Opt. Express* **21** 24385–97
- [11] Wielgus M, Patorski K, Etchepareborda P and Federico A 2014 Continuous phase estimation from noisy fringe patterns based on the implicit smoothing splines *Opt. Express* **22** 10775–91
- [12] Wielgus M and Patorski K 2011 Evaluation of amplitude encoded fringe patterns using the bidimensional empirical mode decomposition and the 2D Hilbert transform generalizations *Appl. Opt.* **50** 5513–23
- [13] Trusiak M, Patorski K and Wielgus M 2012 Adaptive enhancement of optical fringe patterns by selective reconstruction using FABEMD algorithm and Hilbert spiral transform *Opt. Express* **20** 23463–79
- [14] Trusiak M, Wielgus M and Patorski K 2014 Advanced processing of optical fringe patterns by automated selective reconstruction and enhanced fast empirical mode decomposition *Opt. Lasers Eng.* **52** 230–40
- [15] Trusiak M, Patorski K and Wielgus M 2014 Hilbert–Huang processing and analysis of complex fringe patterns *Proc. SPIE* **9203** 92030K
- [16] Trusiak M, Patorski K and Pokorski K 2013 Hilbert–Huang processing for single-exposure two-dimensional grating interferometry *Opt. Express* **21** 28359–79
- [17] Trusiak M, Służewski Ł and Patorski K 2016 Single shot fringe pattern phase demodulation using Hilbert–Huang transform aided by the principal component analysis *Opt. Express* **24** 4221–38
- [18] Larkin K G, Bone D J and Oldfield M A 2001 Natural demodulation of two-dimensional fringe patterns. I. General background of the spiral phase quadrature transform *J. Opt. Soc. Am. A* **18** 1862–70
- [19] Xiong L and Jia S 2009 Phase-error analysis and elimination for nonsinusoidal waveforms in Hilbert transform digital-fringe projection profilometry *Opt. Lett.* **34** 2363–5
- [20] Pan B, Kemaq Q, Huang L and Asundi A 2009 Phase error analysis and compensation for nonsinusoidal waveforms in phase-shifting digital fringe projection profilometry *Opt. Lett.* **34** 416–8
- [21] Herráez M A, Burton D R, Lalor M J and Gdeisat M A 2002 Fast two-dimensional phase-unwrapping algorithm based on sorting by reliability following a noncontinuous path *Appl. Opt.* **41** 7437–44
- [22] Zhu X, Chen Z and Thang C 2013 Variational image decomposition for automatic background and noise removal of fringe patterns *Opt. Lett.* **38** 275–7
- [23] Zhu X, Tang C, Li B, Sun C and Wang L 2014 Phase retrieval from single frame projection fringe pattern with variational image decomposition *Opt. Lasers Eng.* **59** 25–33
- [24] Chen X, Tang C, Li B and Su Y 2016 Variational image decomposition for estimation of fringe orientation and density from electronic speckle pattern interferometry fringe patterns with greatly variable density *Opt. Lasers Eng.* **86** 197–205
- [25] Li B, Tang C, Zhu X, Chen X, Su Y and Cai Y 2016 A 3D shape retrieval method for orthogonal fringe projection based on a combination of variational image decomposition and variational mode decomposition *Opt. Lasers Eng.* **86** 345–55
- [26] Aebischer H A and Waldner S 1999 A simple and effective method for filtering speckle-interferometric phase fringe patterns *Opt. Commun.* **162** 205–10
- [27] Huang N E, Sheng Z, Long S R, Wu M C, Shih W H, Zeng Q, Yen N C, Tung C C and Liu H H 1998 The empirical mode decomposition and the Hilbert spectrum for non-linear and non-stationary time series analysis *Proc. R. Soc. Lond. A* **454** 903–95
- [28] Rudin L, Osher S and Fatemi E 1992 Nonlinear total variation based noise removal algorithms *Physica D* **60** 259–68
- [29] Vese L and Osher S 2003 Modeling textures with total variation minimization and oscillating patterns in image processing *J. Sci. Comput.* **19** 553–72
- [30] Aujol A and Chambolle A 2005 Dual norms and image decomposition models *Int. J. Comput. Vision* **63** 85–104
- [31] Chambolle A 2004 An algorithm for total variation minimization and applications *J. Math. Imaging Vis.* **20** 89–97
- [32] Lim W 2010 The discrete shearlet transform: a new directional transform and compactly supported shearlet frames *IEEE Trans. Image Process.* **19** 1166–80
- [33] Zhang C, Ren W, Mu T, Fu L and Jia C 2013 Empirical mode decomposition based background removal and de-noising in polarization interference imaging spectrometer *Opt. Express* **21** 2592–605
- [34] Salbut L, Patorski K, Jozwik M, Kacperski J, Gorecki C, Jacobelli A and Dean T 2003 Active micro-elements testing

- by interferometry using time-average and quasi-stroboscopic techniques *Proc. SPIE* **5145** 23–32
- [35] Vargas J, Quiroga J A and Belenguer T 2011 Phase-shifting interferometry based on principal component analysis *Opt. Lett.* **36** 1326–8
- [36] Cuhe E, Bevilacqua F and Depeursinge C 1999 Digital holography for quantitative phase-contrast imaging *Opt. Lett.* **24** 291–3
- [37] Trusiak M, Mico V, Garcia J and Patorski K 2016 Quantitative phase imaging by single-shot Hilbert–Huang phase microscopy *Opt. Lett.* **41** 4344–7
- [38] Picazo-Bueno J A, Trusiak M, Garcia J, Patorski K and Mico V 2018 Hilbert–Huang single-shot spatially multiplexed interferometric microscopy *Opt. Lett.* **43** 1007–10
- [39] Patorski K and Olszak A 1997 Digital in-plane electronic speckle pattern shearing interferometry *Opt. Eng.* **36** 2010–5